RESEARCH ARTICLE

Unsteady aerodynamic forces estimation on a square cylinder by TR-PIV

D. F. Kurtulus · F. Scarano · L. David

Abstract The unsteady aerodynamic forces acting on a square cross-sectional cylinder are investigated by means of time-resolved particle image velocimetry (TR-PIV) at Reynolds number 4,900. The objective of the investigation is to prove the feasibility of non-intrusive force measurements around two-dimensional bodies. The PIV measurements performed at a rate of 1 kHz enable a time resolved (TR) description of the vortex shedding phenomenon occurring at 10 Hz and to follow the time evolution of vortex dominated wake. The instantaneous aerodynamic force coefficients are obtained from the integration of the force equations within a control volume enclosing the object. The required instantaneous pressure distribution is inferred making use of two physical models: Bernoulli relation is adopted in the potential slowly-evolving flow region; in the turbulent wake, the Navier–Stokes equations are invoked to determine the pressure gradient spatial distribution, which integrated in space yields the pressure distribution. The spatial acceleration field is directly obtained from the temporal difference of the time-filtered velocity field. For a choice of the control volume approximately one model height away from the surface the contributions to the aerodynamic forces coming from the different terms of the force equation are individually examined. The convective term dominates the unsteady lift forces whereas the pressure term prevails for the drag. The temporal evolution of C_L returns a clear periodic pattern in phase with the vortex shedding at a frequency of 10.1 Hz (Strouhal number $St = 0.128$) with oscillation amplitude of 0.9, whereas C_D barely shows periodicity. The measurement uncertainties associated to the evaluation of all the terms in the force equation and especially in relation to TR-PIV measurements are discussed.

D. F. Kurtulus
Laboratoire d'Etudes Aérodynamiques,
ENSMA avenue Clément Ader, BP40109,
86961 Futuroscope Chasseneuil, France

D. F. Kurtulus (✉)
Aerospace Engineering Department,
Middle East Technical University,
06531 Ankara, Turkey
e-mail: dfunda@ae.metu.edu.tr

F. Scarano
Department of Aerospace Engineering,
Delft University of Technology, Kluyverweg 1,
2629 HS Delft, The Netherlands

L. David
Laboratoire d'Etudes Aérodynamiques,
SP2MI Université de Poitiers Boulevard Marie et Pierre
Curie, BP30179, 86962 Futuroscope Chasseneuil, France

1 Introduction

The flow properties around bluff bodies such as circular and rectangular cylinders are highly complex and are widely investigated in literature. A detailed flow field description around circular cylinders can be found in Zdravkovich (1997). At Reynolds numbers in the order of 100 the Karman vortex street dominates the wake unsteadiness with periodic shedding of counter-rotating spanwise aligned vortices. As a consequence of the unsteady separation and coherent vortex shedding, the aerodynamic loads also exhibit an unsteady behaviour, which is of concern in wind engineering applications, vehicle aerodynamics, aircraft flutter and acoustic emissions.

The low-Reynolds flow regime around bluff bodies has been extensively investigated by means of 2D and 3D simulations with Direct Numerical Simulations (DNS). Flow field past a square cylinder is investigated for moderate Reynolds numbers ($Re = 150$–500, Sohankar et al. 1999). Shiau et al. (1999) used 2D numerical simulations to examine square cylinder instabilities for low Re numbers, where they concluded that as $Re > 320$, the system could change from bi-stability which maintains the spatial symmetry with a periodic lift coefficient, to tri-stability, which breaks the spatial symmetry resulting in a non-periodic lift coefficient with a non-zero mean. Davis and Moore (1982) investigated numerically 2D flow around rectangles for Re numbers from 100 to 2,800 and the resulting Strouhal numbers were comparable to those from wind-tunnel tests for Re numbers less than 1,000. Hémon and Santi (2004) focused their numerical investigation on the perturbation of vortex shedding in order to decrease the amplitude of vibration at lock-in. Their model is based on 2D Navier–Stokes equations without turbulence modelling using Lagrangian–Galerkin method for $Re = 3,500$. At higher Reynolds numbers of $Re = 2 \times 10^4$, a DNS study has been performed by Saha et al. (2001) and Large Eddy Simulation (LES) solutions are obtained with less computational requirements at $Re = 2.2 \times 10^4$ by Sohankar et al. (2000).

The flow properties of rectangular section bluff bodies have also been investigated experimentally in terms of Strouhal–Reynolds number relationship, aspect ratio, cross-section geometry (rectangular cylinders or prismatic shapes), and incidence angle (Bearman and Obasaju 1982; Okajima 1982; Luo et al. 1994; Shinmada and Ishihara 2002). Okajima (1982) showed that the Strouhal number for a square cylinder situated in a uniform flow with 0.5% free stream turbulence is constant and equal to 0.133 for Reynolds number between 1,000 and 20,000. Laser Doppler Velocimetry (LDV) (Durao et al. 1988 for $Re = 14,000$; Lyn et al. 1995 for $Re = 22,000$) has been used to measure the velocity fluctuation components. Lyn et al. (1995) measured the Strouhal number to be 0.132 ± 0.004 for $Re = 21,400$. Particle Image Velocimetry (PIV) measurements around square cylinders were used to obtain the planar velocity field. A Proper Orthogonal Decomposition (POD) analysis was used to extract the modes of the flow from PIV measurements and to obtain a phase reconstruction of the velocity field evolution (van Oudheusden 2005; Roosemboom 2005).

A review of experimental measurements of fluctuating lift on a stationary cylinder is given by Norberg (2003), who also provides a comparison of Strouhal number and sectional rms lift coefficient obtained with two and 3D simulation data in the literature. Berton et al. (2004) estimated different terms in the momentum and Bernoulli equations using the velocity field only (obtained with LDV) in order to determine the airload components acting on the blade section of helicopter rotors in forward flight. PIV has already been proposed for the non-intrusive evaluation of aerodynamic forces. Unal et al. (1998) used a momentum-based approach to determine the instantaneous force on a circular cylinder. Two methods based on the Lagrangian and the Eulerian specifications are compared by Jakobsen et al. (1997) using a four-CCD-camera system to predict the acceleration field from velocity measurements in wave phenomena. In the Eulerian description of fluid motion all variables are taken to be functions of time and local position, rather than initial position as in the case of Lagrangian description. Liu and Katz (2003) use four-exposure PIV to measure the material acceleration of the flow, and by integration, deduce it to obtain the pressure distribution for a 2D cavity flow field. The Poisson equation is used by Gurka et al. (1999) to obtain the pressure field from the PIV velocity field in the stagnation region of an impinging jet and the same equation is used by Fujisawa et al. (2005) to get the pressure field and aerodynamic forces for a circular cylinder at $Re = 2,000$. Tan et al. (2005) use the flux equation introduced by Noca et al. (1999) for force predictions around circular cylinder at $Re = 150$ and 260 and emphasized that predictions are generally better when the integration boundary is closer to the cylinder.

Most studies concentrating on aerodynamic force evaluation are done for experiments in water flows and at relatively low Re number. However, it is of engineering interest to increase the Reynolds number of such experiments as well as moving from water to air as working fluid. In this case the measurement conditions become more critical since high-repetition rate (typically kHz) PIV systems have to be employed with a significant drop in laser pulse energy resulting in a low signal-to-noise ratio during cross-correlation analysis as well as significant peak-locking effects.

The objective of the present study is to provide time-resolved measurements of aerodynamic force coefficients using PIV data around a square cylinder, which has not been yet proposed in the literature. The focus is on the characterization of the unsteady flow around a square cylinder first and then on the determination of the flow-induced unsteady forces on the bluff body with time-resolved particle image velocimetry (TR-PIV). The study also proposes a

robust procedure to evaluate the pressure field from planar velocity and acceleration field. This is performed by selecting Bernoulli equation or the Navier–Stokes equations for different regions of the flow domain.

2 Force estimation by PIV

2.1 Governing equations

A momentum balance written in integral form for a fixed control volume V delimited by the control surface S including the object under investigation (Fig. 1) yields the aerodynamic force (Eq. 1, left) acting on it. Newton's second law dictates that the time rate of change of momentum within V (the right-hand side of the Eq. 1) equals the net force. The latter originates from viscous and normal stresses (shear and pressure, respectively) acting on the model surface (fourth and third term of Eq. 1, right). The balance evaluated away from the model surface must also take into account the rate of change of momentum due unsteady variations of the momentum within V (first term in Eq. 1, right) and that due to convection across S (second term in Eq. 1, right).

$$\vec{F}(t) = -\rho \iiint_V \frac{\partial \vec{V}}{\partial t} dV - \rho \iint_S \left(\vec{V} \cdot \vec{n} \right) \vec{V} dS$$
$$- \iint_S p\vec{n}dS + \iint_S \bar{\bar{\tau}}\vec{n}dS \qquad (1)$$

where $\vec{n}$ denotes the normal direction of the control surface, ρ the fluid density, $\vec{V}$ the velocity vector and $\bar{\bar{\tau}}$ the viscous stress tensor.

A rectangular control volume of unit depth is chosen (as shown in Fig. 1) and net fluxes are calculated across
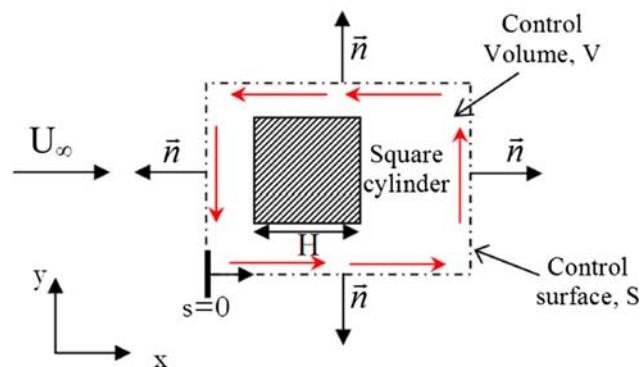
Fig. 1 Control volume and control surface definitions around the square cylinder

its boundary. The terms on the right-hand side of Eq. 1 can all be obtained experimentally from time-resolved PIV measurements, except for the static pressure, which needs to be inferred from the Navier–Stokes equations as shown in Eq. 2. The velocity total derivative (derivative following a fluid particle, left-hand side term of Eq. 2) is obtained as a sum of the Eulerian acceleration (unsteady term) and the convective term (Euler term).

The momentum equations in differential form (Eq. 2) yield the pressure gradient. The term containing the Laplacian of the velocity accounts for momentum viscous diffusion.

$$\frac{D\vec{V}}{Dt} = -\frac{1}{\rho}\nabla p + v\nabla^2 \vec{V} \qquad (2)$$

In a first approach, the integration inside the control volume reduces to the integration inside a 2D domain assuming unit depth and the integration along the boundaries of the control surface S transforms to a counter-clockwise contour integration around a unit depth surface. The third velocity component cannot be evaluated from the present experiments, which report only the unsteady 2D effects on the unsteady loads. The contribution of viscous stresses can in practice be neglected if the control volume is sufficiently far from the body as also verified in the remainder of the paper. Using $\vec{n}dS = [dy \quad -dx]^T$ and $\vec{F} = [D \quad L]^T$, where D and L are the drag and lift force, respectively, the force equation (Eq. 1) can be written as:

$$\begin{bmatrix} D \\ L \end{bmatrix} = -\rho \iint_V \begin{bmatrix} \frac{\partial u}{\partial t} dx\,dy \\ \frac{\partial v}{\partial t} dx\,dy \end{bmatrix} + \rho \oint_S \begin{bmatrix} -u^2\,dy + uv\,dx \\ -uv\,dy + v^2\,dx \end{bmatrix}$$
$$+ \oint_S \begin{bmatrix} -p\,dy \\ p\,dx \end{bmatrix} \qquad (3)$$

The first component on the right-hand side of Eq. 3 is the unsteady term (t), calculated by the spatial integration of the acceleration field within the control volume. The second term corresponds to the momentum convective flux (m) and last term is the contribution due to the fluid pressure p.

The evaluation of the aerodynamic force coefficients C_D and C_L per unit span are done by the normalization of the drag and lift coefficients with respect to the free stream velocity (U_∞) and the lateral dimension of the square cylinder (H). Equation 4 also shows on the right-hand side the decomposition of the unsteady (t), convective (m) and pressure (p) contribution, respectively.

$$\begin{bmatrix} C_D \\ C_L \end{bmatrix} = \begin{bmatrix} \frac{D}{(1/2\rho U_\infty^2 H)} \\ \frac{L}{(1/2\rho U_\infty^2 H)} \end{bmatrix} = \begin{bmatrix} C_{Dt} \\ C_{Lt} \end{bmatrix} + \begin{bmatrix} C_{Dm} \\ C_{Lm} \end{bmatrix} + \begin{bmatrix} C_{Dp} \\ C_{Lp} \end{bmatrix} \quad (4)$$

2.2 Evaluation of pressure distribution

The Navier–Stokes equations can be used to obtain the pressure distribution along the control surface by spatial integration of the pressure gradient as shown in Eq. 6. The process of spatial integration is known to suffer from error propagation, therefore a specific procedure is chosen to limit the latter effect using an additional flow model for the determination of the pressure. Outside of the viscous wake, the pressure can be estimated from potential flow theory:

$$P(s) = \frac{\partial \phi}{\partial t} + P_0 - \frac{1}{2}\rho \left| \vec{V}(s) \right|^2 \quad (5)$$

where the value of P_0 is the total pressure in the free-stream usually obtained from a Pitot measurement device placed in the free stream. A simplified quasi-steady form of the Bernoulli equation is adopted neglecting the contribution of the potential function time derivative (first term in Eq. 5, right).

In the wake, the inviscid steady hypothesis clearly does not apply and the pressure gradient obtained from the Navier–Stokes equations needs to be integrated between two boundary points at the edges of the wake (Fig. 2). The advantage of such procedure with respect to the integration of the pressure gradient along the entire contour S is that undesired error propagation associated with the integration of the pressure gradient (affected by measurement error) is strongly limited to a smaller region of the flow domain as also discussed in Sect. 4.2:

$$P(s) = P(s - \Delta s) + \vec{\nabla} p(s) \cdot \mathrm{d}\vec{s} \quad (6)$$

The pressure in non-dimensional form is the pressure coefficient C_p defined as:
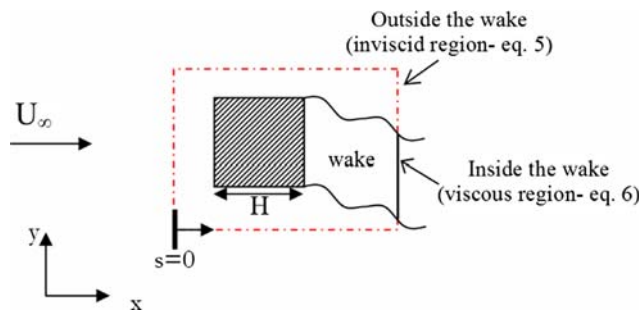
Fig. 2 Inviscid and viscous region definitions along the control surface

$$C_P = \frac{P - p_\infty}{\frac{1}{2}\rho U_\infty^2} \quad (7)$$

where U_∞ and p_∞ are free stream velocity and free stream static pressure, respectively.

The aerodynamic force coefficients are evaluated for a rectangular control volume. The Eulerian acceleration is obtained by differentiating the velocity field in time and then spatially integrating over the 2D volume, whereas the momentum and pressure terms are integrated along a contour marking the boundary.

## 3 Experimental apparatus and procedure

3.1 Flow facility and diagnostic apparatus

The experimental setup for the time resolved PIV measurements is represented in Fig. 3. A uniform stream with background turbulence intensity below 0.5% is produced in the closed-loop low speed wind tunnel of LEA.

The test section has slightly diverging side-walls in order to compensate for the boundary layer growth. A square cylinder of 30 mm height and aspect ratio of 17 is manufactured in Plexiglas with a hollow region in the median section in order to minimise light block due to total reflection inside. The measurements are performed on the symmetry plane.

Seeding particles of 1 μm median diameter are produced from a fog machine and continuously introduced in the circuit until optimal seeding concentration is attained.

A double cavity Quantronix Nd:LYF laser delivers 18 mJ per pulse at 1.0 kHz. The light sheet thickness is
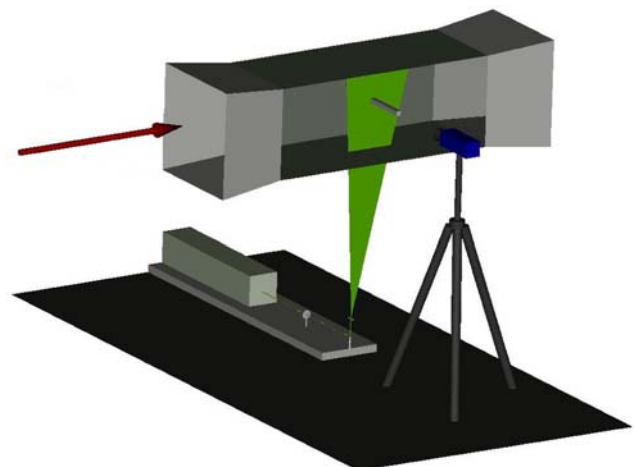
Fig. 3 Experimental setup for TR-PIV measurement

approximately 1 mm. The light scattered by the particles is recorded with a Photron CMOS camera (1,024 × 1,024 pixels, pixel size = 17 μm) at a rate of 1,000 double images per second, with a time separation between exposures of 300 μs. The camera equipped with a 105 mm Nikkor lens is set at $f\#$ = 2.8 imaging a field of view (FOV) of 13.5 × 13.5 cm². The recordings are analysed with the WIDIM technique (Scarano and Riethmuller 2000) with interrogation windows of 31 × 31 pixels and 75% overlap factor.

A time-enhanced analysis is performed in order to make use of recordings acquired at two different time steps 0.3 and 1.3 ms, respectively. A first robust analysis performed on the shorter separation produces a displacement predictor for the image deformation to be applied for the longer time separation image analysis. The advantage of the larger time separation is that the dynamic range of the measurement can be increased in regions where spatio-temporal velocity fluctuations are small and fall below the measurement detectability, which is a specific problem for high-repetition rate systems operating in a critical particle imaging regime (d_p ~ 0.5 pixels) where peak-locking is unavoidable.

A reduction of time-uncorrelated noise is achieved applying a second-order least-squares regression of the velocity data in time with a sliding kernel of 5 ms (five exposures). The experimental parameters are summarized in Table 1.

3.2 Data reduction

The incompressible Navier–Stokes equations are numerically integrated using the unsteady velocity field obtained from TR-PIV. The calculations are achieved by means of a finite difference method on a cartesian grid of 124 × 124 points. Central differences in space and time have been chosen in order to achieve second-order accuracy. All variables are therefore evaluated at time $t_a = t + \Delta t/2$. The Eulerian acceleration term is calculated by central difference at time t_a, over a time interval of $3\Delta t$. Finally, the pressure gradient components are calculated in the wake region from the momentum equation (Eq. 2).

The distinction between viscous and inviscid flow region is made on the basis of the local absolute vorticity. The inviscid flow region is identified as that with a vorticity level more than one order of magnitude below the typical vorticity fluctuation exhibited in the turbulent wake. The viscous wake is identified as a compact domain avoiding that local instantaneous minima in the vorticity due to the fine-scale turbulent structure of the flow and due to sign reversal are interpreted as patches of inviscid flow. This is achieved low-pass filtering the vorticity spatial distribution, which diffuses the absolute vorticity field and sets the boundaries of the integration conservatively towards the outside of the required region. The space-marching integration takes as initial value the static pressure returned by the Bernoulli equation. The end point of the integration is compared with the value given by the Bernoulli equation and the discrepancy is redistributed with a linear weighting function along the entire integration domain.

4 Results

4.1 Instantaneous flow dynamical evolution

The shedding of spanwise vortices with a long coherence length is the dominant phenomenon governing the unsteady forces exciting periodically the square cylinder. The instantaneous velocity contours are plotted during the observation time that covers one-quarter of the shedding cycle.

Introducing the non-dimensional time $t^* = t/T$ where T is the shedding period, the velocity field at $t^* = 0.25$ (minimum lift), $t^* = 0.5$ (zero lift) and $t^* = 0.75$ (maximum lift) is represented in Fig. 4. The blank area around the square cylinder is due to the perspective effect obstructing the complete view of the flow close to the model surface.

The instantaneous velocity vector field exhibits a large region close to the rear face of the object where reverse flow occurs. On the side walls, the flow separates at the leading corners and only reattaches at the end of the separated wake. It can also be observed that the instants $t^* = 0.25$ and $t^* = 0.75$ correspond to the growth phase of the clockwise vortex at the upper trailing corner and counter-clockwise vortex at the lower trailing corner, resulting in a negative and positive lift coefficient peaks, respectively. At $t^* = 0.75$, the wake shows a separated clockwise vortex and the high positive lift value is associated to the vigorous downwash.
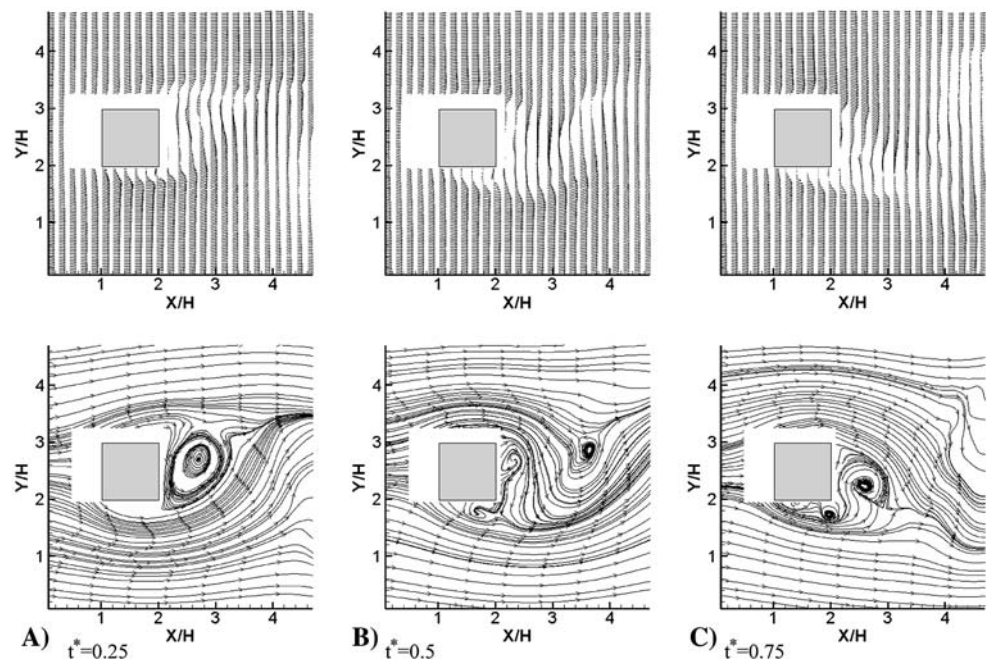
From the streamline analysis the following can be inferred (Fig. 4, bottom): a large counter-clockwise vortex increases its strength at the base of the square at $t^* = 0.25$, while the clockwise vortex is being formed at the upper side. When this dominant vortex detaches and moves downwards its interaction with the flow upstream attracts the clockwise vortex towards the base for its growth. At this time instant, a new counter-clockwise vortex is visible at the lower side and by the time $t^* = 0.75$, the vortex shed from the upper corner

Table 1 Flow properties and PIV parameters

|	
Bluff body	
Height, H [mm]	30
Aspect ratio	1:17
Flow	
Fluid	Air
Re	4,890
U_∞ [m/s]	2.37
Seeding	
Type	Smoke
Concentration [1/mm^3]	10
Diameter [μm]	1
Laser	
Type	Nd:YLF
Thickness [mm]	1
Pulse energy [mJ/pulse]	18
Recording	
Camera type	CMOS Photron
Objective focal length [mm]	105
F number	2.8
Recording rate [Hz]	1,000
Dynamic range	10 bit
Δt [μs]	1,000
FOV [mm^2]	145 × 145
Image magnification	0.12
Exposure delay time [μs]	300
Max. particle displacement	8 px
Interrogation	
Method	Window deformation iterative multigrid

grows and dominates the base wake of the square. This process is cyclical and dominates the unsteady wake behaviour.

Moreover, at the current value of the Reynolds number, the free shear layers separating from the sharp leading edges undergo instability forming Kelvin–Helmholtz type rollers, which are then entrained and merged within the roll-up of the Kármán vortices.

In order to illustrate the relation between the unsteady loads and the physical behaviour of the wake flow, the fundamental and derived kinematic flow properties (velocity, vorticity and Eulerian acceleration), and the pressure gradient field are displayed in Fig. 5.

The first column from the left displays the velocity magnitude, the vorticity is shown in the second column and in the third column magnitude of the acceleration vector is plotted. The last column returns the spatial distribution of the pressure gradient magnitude as obtained from Eq. 2. This enables a comparison between the velocity field, the acceleration field and indirectly the pressure distribution. At $t^* = 0.25$ the counterclockwise rotating vortex induces a significant asymmetry of the velocity field with a higher flow velocity on the bottom side of the cylinder due to the higher streamline curvature induced at the bottom-leading edge. The corresponding acceleration field returns appreciable activity only in the turbulent wake with peaks approximately within the growing vortex. The pressure gradient distribution shows clear peaks in proximity of the leading edges associated with the flow acceleration around the sharp corners. High levels of the pressure gradient also correlate with the vortex core region and to a minor extent to the separated

**Fig. 4** Instantaneous velocity vectors and streamlines
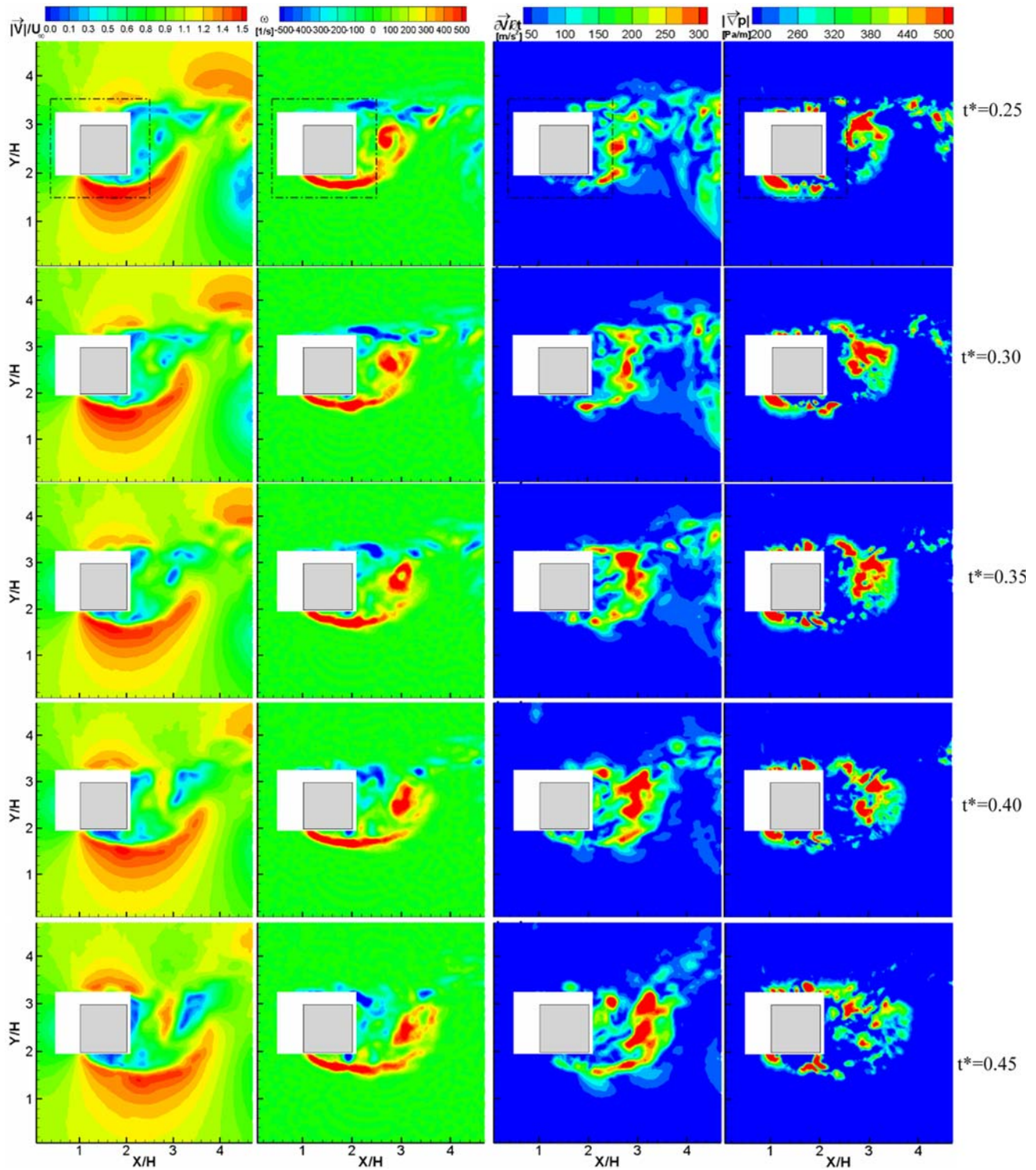
Fig. 5 Instantaneous velocity, vorticity, Eulerian acceleration and pressure gradient magnitudes at different time instants

shear layers where small vortices are being formed as a consequence of shear layer instability. The time evolution of the above discussed features shows that far from the object the fluctuating flow properties are advected at approximately uniform speed, whereas close

to the cylinder base, the vortex-related flow properties have a longer residence time associated to the formation and growth process. The diffusive terms are not plotted for sake of conciseness since their contribution in the momentum equation is more than two orders of

Fig. 6 Instantaneous velocities and Eulerian acceleration magnitudes along the control surface
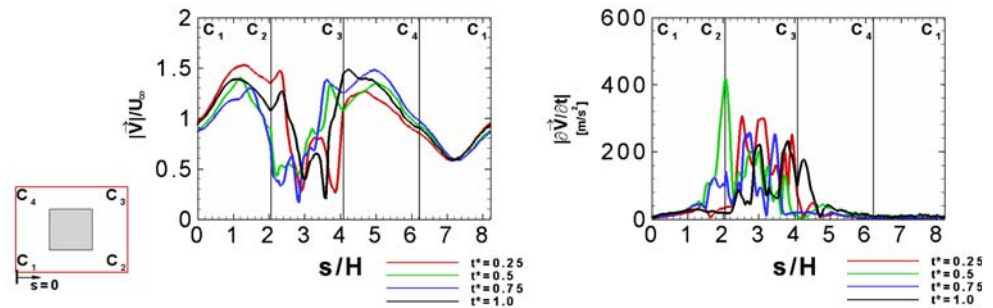
Fig. 7 Instantaneous pressure gradient magnitudes and pressures along the control surface at different time instances
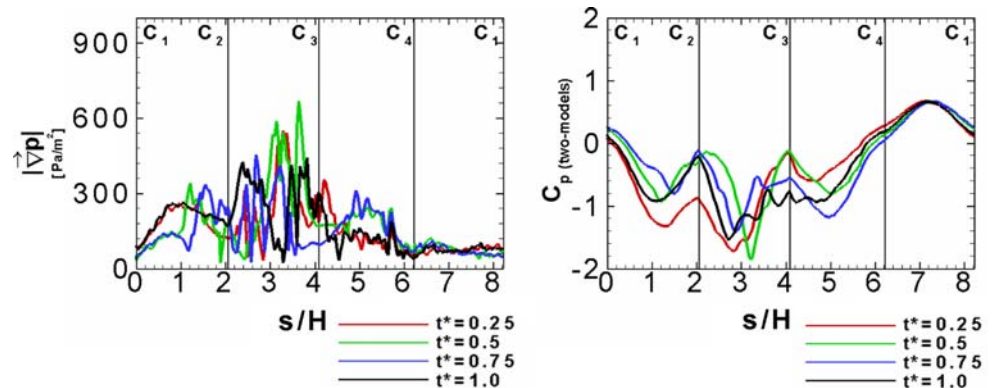
magnitude below the Euler terms except for a small region close to the object leading edges where the shear layers separate.

4.2 Flow properties on the control surface

The instantaneous velocity and acceleration magnitude at several time instants along the contour are represented in Fig. 6. The velocity shows significant time variations both inside and outside the wake, with smaller scale structures in the wake. Given the large difference in time and length scales of the fluctuations in the outer flow and in the wake, the level of acceleration in the outer flow becomes practically negligible with respect to that inside the turbulent wake. Combining the acceleration and the Euler terms yields the total derivative (Eq. 2), which is found to be almost equal and opposite to the pressure gradient term. This indicates that their sum given by the diffusive term in the momentum equation is negligible in the balance. The time derivative of the velocity along the contour is close to zero in the inviscid region and reaches the same order of magnitude as the total derivative only in the viscous region. It could be concluded that the Euler term dominates the total derivative in the inviscid flow region.

In Fig. 7, the pressure gradient magnitudes and pressure coefficient obtained after integration along

the contour are displayed at four different time instants. The instantaneous pressure gradient profile exhibits non-zero values also in the inviscid flow region and more pronounced small scale fluctuations within the turbulent separated wake. The pressure coefficient appears rather constant upstream of the cylinder (interval C_4–C_1) and time fluctuations reach a maximum at the cylinder base as expected (interval C_2–C_3).

To highlight the importance of adopting two different models for the eduction of the pressure from the velocity measurements, the static pressure distribution along the control surface at three different time instants is displayed in Fig. 8. On the left side, the polar plot shows with black lines the pressure obtained after the integration of the pressure gradient (Eq. 6) across the viscous wake region (Fig. 2), whereas the red line indicates the static pressure as obtained from the steady Bernoulli equation (Eq. 5). Clearly the Bernoulli model is inadequate within the wake yielding a higher pressure level since total pressure losses are not taken into account. On the right-hand side of the figure, pressure diagrams are presented along the curvilinear abscissa. The blue lines indicate the result obtained when the integration process is performed along the entire control surface irrespective of the inviscid or viscous character of the flow.

Two main conclusions can be drawn: (a) the pressure obtained from the Bernoulli equation is generally

in good agreement with that obtained from the integration of the Navier–Stokes equations, meaning that the inviscid quasi-steady flow hypothesis holds outside of the viscous wake and at the same time error propagation is not very crucial; (b) under some circumstances, local errors introduced in the integration of the pressure gradient (e.g. Fig. 8 bottom-right) do propagate making the space-marching integration process depart from the actual value of the pressure outside of the viscous region. This justifies the adoption of the two-models approach as being at the same time robust with respect to localized errors and accurate and physically consistent in the turbulent wake.

4.3 Aerodynamic force coefficients

The integration of the force equation terms (c_L, c_D) along the control surface and the integration of the unsteady term within the control volume return the aerodynamic force coefficients (C_L, C_D). The individual contributions to the force from the momentum convection and from the pressure distribution are denoted with "m" and "p", respectively, and the elemental contribution is taken along the abscissa s (Fig. 9). The contribution to lift from the momentum convection is antisymmetrical in front of the cylinder and approximately symmetrical on the sides where it varies smoothly. In the wake, the contribution to lift shows the largest spatial and temporal fluctuations.

The contribution to drag force is mostly due to the unbalance between front and rear region of the contour, respectively. In this specific case the momentum contribution only would yield a negative drag, which is purely due to the proximity of the control surface to the model. In fact, when the control surface approaches the model surface the pressure terms becomes the dominating component in the force equation. The lift and drag contribution from the pressure distribution are non-zero only along the portions of control surface normal to the force component. The pressure contribution to the aerodynamic force shows less relative fluctuations in space and time, but the overall value is higher than the momentum term. The pressure term therefore dominates the drag at such distance from the model. The proposed representation of the contribution to the total lift and drag distributed along the control surface cannot be applied for the unsteady term (denoted by "t"), which is a volume integral and is represented in Fig. 10 as a function of time together with the momentum and pressure terms composing the overall force coefficient.

It is observed that the vortex at the trailing lower side of the control volume at $t^* = 0.25$ (red line,

negative peak location close to the corner C_2, Fig. 9a) and at the upper side of the control volume at $t^* = 0.75$ (blue line, positive peak location close to corner C_3, Fig. 9a) introduces a specific pattern for the momentum term, with an anti-symmetric profile and an inflexion point with two peaks of opposite signs in the profile. At $t^* = 0.5$ and $t^* = 1.0$ an approximately neutral line replaces the previous pattern. The mean time lift coefficient only due to the momentum term is $\langle C_{Lm} \rangle = 0.154$, while its rms time fluctuation is 0.758.

The time evolution of the lift coefficient is shown in Fig. 10, left (black line). The unsteady, convective and pressure terms are given by red, green and blue lines, respectively. A clearly periodic pattern is exhibited by all components with convective and pressure terms having the same phase which oppose to unsteady term phase. The average amplitude reached by the fluctuations of the lift coefficient is 1.5 with a period $T = 99$ ms. The diagram of the time evolution of the unsteady term is, however, still affected by noisy fluctuations ascribed to spurious vectors within the measurement volume.

The periodicity of the drag coefficient is barely visible in the diagram of its time evolution. The pressure term clearly dominates the drag, whereas the contribution of the unsteady term is centred on zero. The contribution from momentum convection is negative and it is approximately half of the pressure term.

Table 2 summarizes the mean and rms of aerodynamic force coefficient time evolution within nine shedding periods.

The lift coefficient C_{Lt} has approximately zero mean and the amplitude of the fluctuations is in good agreement with the literature data ($\langle C_{Lmax} \rangle = 1.5$). The mean value of the drag coefficient is $\langle C_D \rangle = 1.5$ which underestimates the expected value of 1.9–2.2 reported by previous studies. This is ascribed to the fact that the drag coefficient is obtained from the subtraction of the convective term from the pressure term and is therefore more sensitive to errors committed either in the velocity measurement or in the pressure evaluation. The rms fluctuation of the drag coefficient is also relatively high approximately 0.5.

Finally, the temporal autocorrelation function applied to the time evolution of the lift and drag coefficient allows a quantitative determination of the periodic flow properties. The period of the vortex shedding is found to be $T = 99$ ms from the autocorrelation of the lift coefficient (represented as black line in Fig. 11, left). This results in a Strouhal number of $St = H/(TU_\infty) = 0.128$, in agreement with Bearman and Obasaju (1982), and Norberg (1993) among others. The cross-correlation of the lift coefficient, confirms

Fig. 8 Instantaneous pressure
coefficients along the
rectangular contour.
Bernoulli equation (*red line*);
Bernoulli equation in the
inviscid flow and N–S
equation in the viscous region
(*black line*); N–S equations
integration everywhere (*blue
line*)
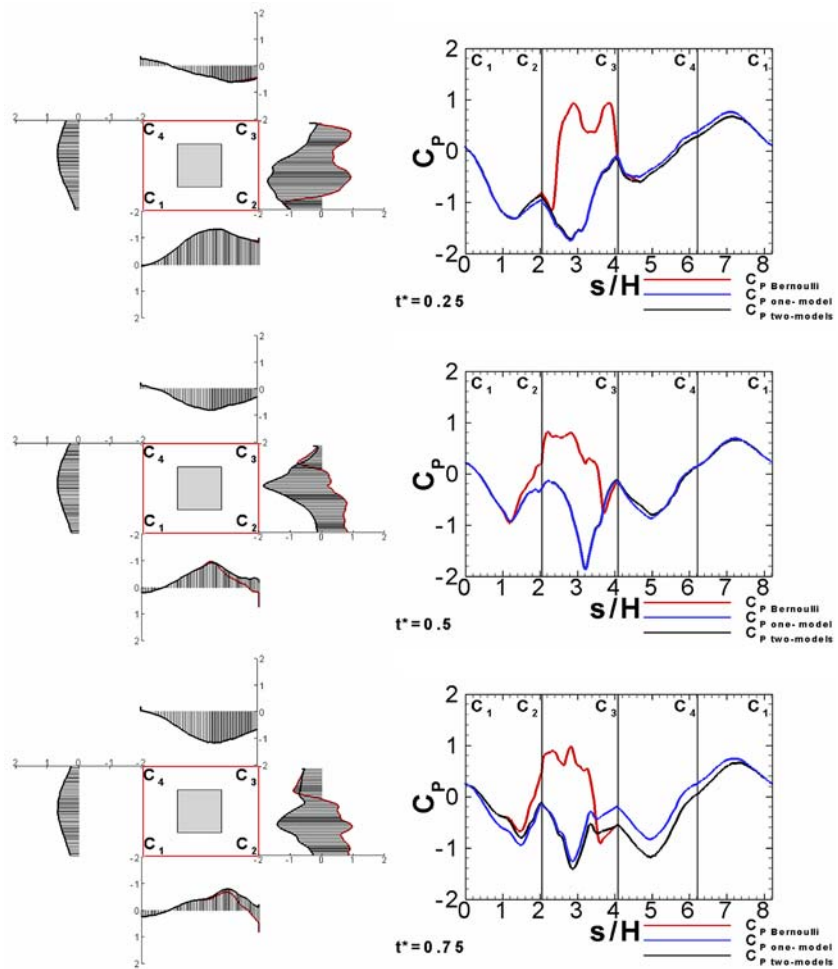
Fig. 9 Elemental momentum
and pressure terms of the
aerodynamic force
coefficients around the
control surface for different
time instants
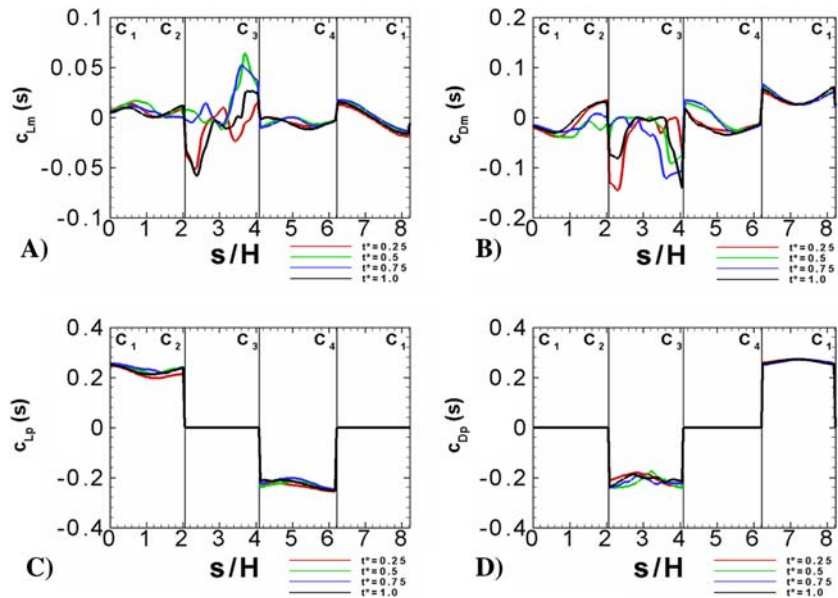
that the momentum and pressure terms, which domi-
nate the lift are out of phase with the unsteady com-
ponent. The autocorrelation of the drag coefficient

time evolution is expected to be periodic with a fre-
quency twice that of the lift coefficient. However, this
expected pattern is not clearly revealed by the auto-

Fig. 10 Unsteady lift and drag coefficients (*black*). Unsteady contribution (*red*); convection term (*green*) and pressure term (*blue*)
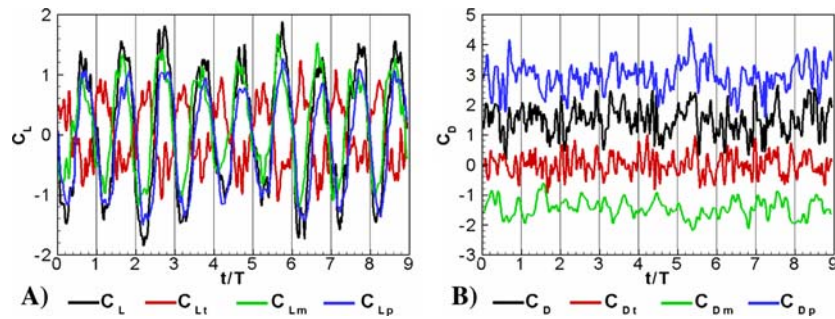
Table 2 Mean and RMS values of aerodynamic coefficients

	Mean	RMS
C_D	1.5	0.48
C_L	0.049	1.033

correlation function (Fig. 11, right). The cross correlation of the pressure term is very close to the auto correlation of the drag coefficient. The periodicity of the drag coefficient could be visualized more or the less with the first three peak locations of the cross correlation of the momentum term with the drag coefficient (green line in Fig. 11, right).

5 Conclusions

Time-resolved PIV measurements are performed to obtain the unsteady forces on a square section cylinder at $Re = 4,890$ in an airflow. The control volume approach is used to evaluate the forces acting on the cylinder. The flow acceleration field is directly obtained from the TR-PIV measurements by finite differences, however, a specific image processing and data post-processing is needed in order to enlarge the measurement dynamic range limited by peak-locking effects intrinsic of high-speed PIV systems. The unsteady pressure gradient field is obtained invoking the Navier–Stokes equations and the pressure is evaluated from a two-model approach, based on the Bernoulli equation (in the inviscid region) and the line integration of the pressure gradient from the complete Navier–Stokes equations inside the turbulent wake. The results show that for bluff-body wakes, the unsteady term can be neglected in the inviscid flow region and that the evaluation of the pressure is actually needed only within the turbulent wake region. Outside of that region convection is the dominant term in the momentum equation. Moreover the viscous term is practically always negligible. The analysis of the time evolution of the lift coefficient returns a clear periodicity, in phase with the phenomenon of vortex shedding. The drag coefficient time evolution shows a less pronounced periodicity. The current study demonstrates that TR-PIV can be used as a non-intrusive measurement technique to evaluate unsteady aerodynamic loads in two-dimensional flows. Further efforts are to be directed towards improving the accuracy of the acceleration field and to estimate the effects of the three-dimensional flow behaviour on the measurement accuracy.

Fig. 11 Temporal auto-correlation and cross-correlation functions of the lift and drag coefficients and their components
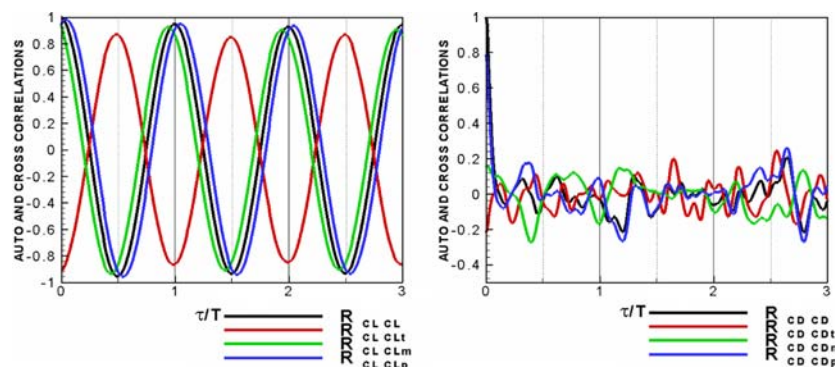
References

Bearman PW, Obasaju ED (1982) An experimental study of pressure fluctuations on fixed and oscillating square-section cylinders. J Fluid Mech 119:297–321

Berton E, Maresca C, Favier D (2004) A new experimental method for determining local airloads on rotor blades in forward flight. Exp Fluids 37:455–457

Davis RW, Moore EF (1982) A numerical study of vortex shedding from rectangles. J Fluid Mech 116:475–506

Durao DFG, Heitor MV, Pereira JCF (1988) Measurements of turbulent and periodic flows around a square cross-section cylinder. Exp Fluids 6:298–304

Fujisawa N, Tanahashi S, Srinivas K (2005) Evaluation of pressure field and fluid forces on a circular cylinder with and without rotational oscillation using velocity data from PIV measurement. Meas Sci Technol 16:989–996

Gurka R, Liberzon A, Hefetz D, Rubinstein D, Shavit U (1999) Computation of pressure distribution using PIV velocity data. In: Proceedings of the third international workshop on PIV'99, Santa Barbara, September 1999, pp 671–676

Hémon P, Santi F (2004) Perturbation of vortex induced vibrations on a square section cylinder. In: de Langre E, Axisa F (eds) Proceedings of the 8th international conference on flow induced vibration, Paris, France, July 2004, vol 2, pp 493–498

Jakobsen ML, Dewhirst TP, Greated CA (1997) Particle image velocimetry for predictions of acceleration fields and force within fluid flows. Meas Sci Technol 8:1502–1516

Liu X, Katz J (2003) Measurements of pressure distribution by integrating the material acceleration. In: Proceedings of the fifth international symposium on cavitation. Osaka, Japan

Luo SC, Yazdani MdG, Chew YT, Lee TS (1994) Effects of incidence and afterbody shape on flow past bluff cylinders. J Wind Eng Ind Aero 53:375–399

Lyn DA, Einav S, Rodi W, Park JH (1995) A Laser-Doppler velocimetry study of the ensemble-averaged characteristics of the turbulent near wake of a square cylinder. J Fluid Mech 304:285–319

Noca F, Shields D, Jeon D (1999) A comparison of methods for evaluating time dependent fluid dynamic forces on bodies, using only velocity fields and their derivatives. J Fluids Struct 13:551–578

Norberg C (1993) Flow around rectangular cylinders: pressure forces and wake frequencies. J Wind Eng Ind Aero 49:187–196

Norberg C (2003) Fluctuating lift on a cylinder: review and new measurements. J Fluids Struct 17:57–96

Roosenboom EWM (2005) Experimental analysis of the flow around a cylinder with a square cross-section, M.Sc thesis, Faculty of Aerospace Engineering, TU Delft, August 2005

Saha AK, Biswas G, Muralidhar K (2001) Two-dimensional study of the turbulent wake behind a square cylinder subject to uniform shear. J Fluids Eng 123:595–603

Scarano F, Riethmuller M (2000) Advances in iterative multi-grid PIV image processing. Exp Fluids 29:51–60

Shiau YH, Peng YF, Hwang RR, Hu CK (1999) Multistability and symmetry breaking in the 2-D flow around a square cylinder. Phys Rev E 60:6188–6191

Shimada K, Ishihara T (2002) Application of a modified k–e model to the prediction of aerodynamic characteristics of rectangular cross-section cylinders. J Fluids Struct 16:465–485

Sohankar A, Norberg C, Davidson L (1999) Simulation of three-dimensional flow around a square cylinder at moderate Reynolds numbers. Phys Fluids 11:288–306

Sohankar A, Davidson L, Norberg C (2000) Large eddy simulation of flow past a square cylinder: comparison of different subgrid scale models. J Fluids Eng 122:39–47

Okajima A (1982) Strouhal numbers of rectangular cylinders. J Fluid Mech 123:379–398

Tan BT, Thompson MC, Hourigan K (2005) Evaluating fluid forces on bluff bodies using partial velocity data. J Fluids Struct 20:5–24

Unal MF, Lin JC, Rockwell D (1998) Force prediction by PIV imaging: a momentum-based approach. J Fluids Struct 11:965–971

Van Oudheusden BW, Scarano F, van Hinsberg NP, Watt DW (2005) Phase-resolved characterization of vortex shedding in the near wake of a square-section cylinder at incidence. Exp Fluids 39:86–98

Zdravkovich MM (1997) Flow around circular cylinders, vol 1. Fundamentals. Oxford University Press, Oxford, ISBN 0-19-856396-5